

# Study of multi-periodic coronal pulsations during an X-class solar flare

Partha Chowdhury<sup>a</sup>, A.K. Srivastava<sup>b</sup>, B.N. Dwivedi<sup>b</sup>, Robert Sych<sup>c</sup>, Y.-J. Moon<sup>a</sup>

<sup>a</sup>*School of Space Research, Kyung Hee University, Yongin, Gyeonggi-Do, 446-701, Korea.*

<sup>b</sup>*Department of Physics, Indian Institute of Technology (Banaras Hindu University), Varanasi-221005, India.*

<sup>c</sup>*Institute of Solar-Terrestrial Physics SB RAS, Irkutsk-664033, Russia.*

---

## Abstract

We investigate quasi-periodic coronal pulsations during the decay phase of an X 3.2 class flare on 14 May 2013, using soft X-ray data from the RHESSI satellite. Periodogram analyses of soft X-ray light curves show that  $\sim 53$  s and  $\sim 72$  s periods co-exist in the 3–6, 6–12 and 12–25 KeV energy bands. Considering the typical length of the flaring loop system and observed periodicities, we find that they are associated with multiple (first two harmonics) of fast magnetoacoustic sausage waves. The phase relationship of soft X-ray emissions in different energy bands using cross-correlation technique show that these modes are standing in nature as we do not find the phase lag. Considering the period ratio, we diagnose the local plasma conditions of the flaring region by invoking MHD seismology. The period ratio  $P_1/2P_2$  is found to be  $\sim 0.65$ , which indicates that such oscillations are most likely excited in longitudinal density stratified loops.

**Keywords:** flares; oscillations; waves; corona; magnetohydrodynamics (MHD)

---



---

*Email addresses:* partha@khu.ac.kr, moonyj@khu.ac.kr (Partha Chowdhury<sup>a</sup>, A.K. Srivastava<sup>b</sup>, B.N. Dwivedi<sup>b</sup>, Robert Sych<sup>c</sup>, Y.-J. Moon<sup>a</sup>), asrivastava.app@iitbhu.ac.in, bnd.app@iitbhu.ac.in, (Partha Chowdhury<sup>a</sup>, A.K. Srivastava<sup>b</sup>, B.N. Dwivedi<sup>b</sup>, Robert Sych<sup>c</sup>, Y.-J. Moon<sup>a</sup>), sych@iszf.irk.ru (Partha Chowdhury<sup>a</sup>, A.K. Srivastava<sup>b</sup>, B.N. Dwivedi<sup>b</sup>, Robert Sych<sup>c</sup>, Y.-J. Moon<sup>a</sup>)

## 1. Introduction

Solar flares are sudden release of magnetic energy occurring in the solar atmosphere, and lasting from a few tens of seconds (impulsive) to a few tens of minutes (gradual). Flare emissions are detected in the entire electromagnetic spectrum, ranging from radio, microwave, visible, ultraviolet, X-rays, hard X-rays, and even to Gamma-rays. The effect of these flares are also detected in the variations of the flux density of solar energetic particles approaching towards the Earth. The electromagnetic radiation generated in solar flares often exhibits oscillatory patterns in the light curves. They are periodic in nature, operating in the flare magneto-plasma, and having typical periods ranging from a few milliseconds to several minutes (Nakariakov & Verwichte, 2005; Nakariakov & Melnikov, 2009; Kim et al., 2012; Kupriyanova et al., 2013; Huang et al., 2014, and references cited therein). These oscillations are referred to as quasi-periodic pulsations (QPPs). In some cases, they have inharmonic shape with apparent amplitude and period modulation (Nakariakov & Melnikov, 2009).

QPPs are classified mainly as short QPPs (sub-second), medium QPPs (seconds to several minutes), and long QPPs (from several minutes to tens of minutes) according to the possible physical mechanisms associated with them (Nakariakov & Melnikov, 2009; Kupriyanova et al., 2010). According to Aschwanden (1987), the short QPPs are probably connected with the interaction of electromagnetic, plasma, or whistler waves with accelerated particles detected in the radio emission. Medium QPPs are likely associated with magnetohydrodynamic (MHD) processes in the solar flaring loops as detected in radio, microwave, white light, and X-ray emissions (Inglis et al., 2008, 2009; Jakimiec & Tomczak, 2008; Asai et al., 2001; Melnikov et al., 2005; Reznikova et al., 2007; McAteer et al., 2005; Reznikova & Shibasaki, 2011, and references cited therein). On the other hand, the long ones are usually relevant to active region (AR) dynamics (Sych et al., 2009, 2015) and global oscillations of the Sun (Tan et al., 2010; Srivastava & Dwivedi, 2010).

QPPs in solar flares are one of the major diagnostic tools to study the physical conditions in flaring sites, and triggering mechanisms. These studies can also be extended to stellar flares, which exhibit QPPs in their radio, optical, and soft X-ray emissions (Mathioudakis et al., 2003; Mitra-Kraev et al., 2005; Pandey & Srivastava, 2009; Anfinogentov et al., 2013; Srivastava et al., 2013). Understanding QPPs during the flare eruption is still an open question. The fundamental physical processes of these oscillations in solar flares are relevant to understanding magnetic reconnection, magnetohydrodynamic (MHD) waves in coronal structures, particle acceleration, thermodynamics, and other kinetic effects. Although the properties of QPPs in solar hard X-ray (HXR) emissions have been widely studied by different researchers, their nature in solar soft X-ray emissions (SXR) in different energy bands simultaneously remains to be extensively investigated. This calls for more observational information from samples with oscillatory behavior in low-energy X-rays.

The ratio of the statistically significant QPPs of the simultaneously existing

spectral components is important for determining the nature and mechanisms of the pulsations both in observations and theory (Van Doorsselaere et al., 2007; Srivastava et al., 2008; Inglis & Nakariakov, 2009; Srivastava & Dwivedi, 2010; Macnamara & Roberts, 2011; Orza & Ballai, 2013; Luna-Cardozo et al., 2012; Erdélyi et al., 2014; Guo et al., 2015, and references cited there). Different periods of QPPs may be associated either with different MHD modes simultaneously present in a flaring loop or with different harmonics of the same MHD mode (Melnikov et al., 2005; Van Doorsselaere et al., 2007; Srivastava et al., 2008; Andries et al., 2009; Inglis & Nakariakov, 2009; Srivastava & Dwivedi, 2010, e.g.).

In this paper, we use the RHESSI data to study the intensity of the co-existing QPPs at 3–6 KeV, 6–12 KeV and 12–25 KeV multiple energy bands during the decay phase of an X-class solar flare on 14 May 2013. In Sect. 2, we briefly present the observations and power spectral analysis methods for detecting QPPs. Sect. 3 describes the results of the QPPs observed in different energy bands of the flaring loop. Exploration of various harmonics of appropriate MHD modes leaving their imprints on selected SXR while excited in the flaring loop system is discussed in Sect. 4. In Sect. 5, MHD seismology of flaring plasma using the observed QPPs are discussed along with conclusions.

## 2. Observations and Analysis Methods

The X 3.2 class solar flare on 14 May 2013 is investigated in the present study. It started at 00:42:39 UT, reached its maximum at 01:07:41 UT, gradually decayed and ended at 03:14:40 UT in GOES SXR observations. Its coordinate at the Sun is N11E74 in an active region NOAA 11748. The flare region is detected by both RHESSI and Nobeyama Radioheliograph (NoRH) in an integrated mode providing flaring light curves in its decay phase in X-rays and radio respectively. Figures 1 (a,b,c) represent some features of this solar flare and related emissions.

Figure 1 (a) shows time profiles of the flare in soft X-rays taken with GOES satellite 1.0–8.0 Å channel and microwave emission during this flare at 17 and 34 GHz observed by NoRH. NoRH provides intensity (Stokes parameter  $I=R+L$ ) and circular polarization (Stokes parameter  $V=R-L$ ) images at 17 GHz with a temporal resolution of 1.0 sec (Nakajima et al. 1994). The fluxes (Figure 1(a), middle panel) and correlation curves (Figure 1(a), bottom panel) at 17 GHz and 34GHz obtained from NoRH vary with the same pattern during the flare process. However, for the flare peak, the 17GHz flux is larger than the 34GHz and afterwards both fluxes become comparable with each other. The radio emission is probably generated by gyro-synchrotron motion of accelerated electrons during the flare peak phase, while in the long decay phase the thermal freefree emissions dominate. The full Sun image obtained from NoRH at 17 GHz (Stokes parameter  $I=R+L$ ) and the corresponding flaring region of the day under study is shown in Figure 1 (b).

Figure 1(c) shows this localized temporal span of the light curve during the decay phase of the flare detected by RHESSI. In these data sets of 3–6 KeV, 6–12 KeV and 12–25 KeV energy bands, best-fit exponential functions of the form  $I = I_0 \times e^{-bt}$  are fitted for the time period between 01:23:40 UT and 01:51:56 UT

to remove the long-term background flare variations and corresponding graphs are shown in Figure 2. For 3–6 KeV energy band, the values  $I_0$  and  $b$  are 349.9 and -0.003996; for 6–12 KeV data set, these values are 4265 and -0.004179; and for 12–25 KeV energy band, the corresponding values are 1960 and -0.005061 respectively.

We have studied the QPPs present in the de-trended signal during the decay phase of the flare by conventional Fast Fourier Technique (FFT), Maximum Entropy Method (MEM) and Lomb-Scargle (LS) periodogram analysis method. The MEM is an alternative method to FFT which avoids the limited resolution and power ‘leaking’, due to the windowing of data, present in the FFT, and it belongs to the class of methods which fit a satisfied model to the data. The parameters of a maximum entropy spectral estimation are equivalent to the ‘ones’ in the auto-regressive (AR) model of a random process in real domain (Burg, 1972).

On the other hand, the Scargle periodogram (Scargle, 1982; Horne & Baliunas, 1986) is an important algorithm for time series analysis of unevenly sampled data. Being quite powerful for finding and testing, the significance of weak periodic signals through false alarm-probability (FAP), a simple estimate of the significance of the height of a peak in power spectrum can be derived. In this method, the confidence levels have been calculated according to the recipe given in Horne & Baliunas (1986). In case of FFT and MEM spectral decomposition techniques, we have calculated the mean ( $\mu$ ) and standard deviation ( $\sigma$ ) of the data points. We have then calculated the confidence levels as  $\mu + 2\sigma = 95.4\%$ ;  $\mu + 3\sigma = 99.7\%$  and  $\mu + 4\sigma = 99.99\%$  respectively. X-axis of FFT, MEM and LS graphs are drawn on a log scale.

In the present study, the periods which are common in all the methods having power  $> 95\%$  confidence levels are considered only for final discussion and calculation. In order to justify the validity of the peaks found from the FFT, MEM and LS methods, the confidence limits for different peaks obtained from the power spectra of different energy bands have been calculated (Haber, 1969; Chowdhury & Ray, 2006; Chowdhury et al., 2009). In every case, confidence levels are above 99%. In effect, we attempt to determine the interval in which any hypothesis concerning the periodicity of a certain solar event might be considered tenable and outside which any hypothesis would be considered untenable. The confidence limits (CL) are evaluated by generating a sample of 100 data points equally on both sides of a particular peak. This method is repeated for all the peaks under consideration within a spectrum. The peak that is sharp gives the minimum value of standard error and closer values of confidence limits.

The confidence interval provides the lower and upper limits to which the population parameter has a high probability of being included. The population parameter standard deviation  $\sigma$  can be calculated from the following formula:

$$\sigma = \{\Sigma T_i^2 / (N - 1) - (\Sigma T_i^2 / N(N - 1))\}^{0.5} \quad (1)$$

Here  $T_i$  represents the  $i$  value of the data under study and  $N$  is the total

number of data points. The standard error  $SE_m$  is the standard deviation of the sample mean (from sampling distribution) which is estimated as:

$$SE_m = \sigma / (N)^{0.5} \quad (2)$$

The confidence limits (CL) for 99% confidence can be computed as

$$CL = T_{ave} \pm 2.58(SE_m), \quad (3)$$

where  $T_{ave}$  is the mean value of the time period of the sample data points.

To determine confidence limits we have used the formula of  $Z_a/2 \times \sigma \sqrt{(n)}$ . Here  $Z_a/2$  is the confidence coefficient,  $a$  is confidence level,  $\sigma$  is standard deviation, and  $n$  is sample size. Then, we have converted the 99 % to a decimal 0.99 and divide it by 2 to get 0.495. According to the table the closest value corresponding to 0.495 is 2.60. Then we have multiplied 2.6 by 0.99 (critical value by our standard error) and we get 2.574 ( $\sim 2.58$ ) and this is our margin of error.

We have then calculated the cross-correlation coefficients (CC) between detrended data of three different energy channels observed by RHESSI to study the time-delay with various time-lags (0,  $\pm 4$ ,  $\pm 8 \dots \pm 50$  seconds). Each of these data sets has been shifted forward or backward and the cross-correlation coefficient has been calculated after shifting the time-lag (L) corresponding to the best correlation of the time phase under investigation. The results are shown in Figures 6 (a,b,c).

### 3. Results

#### 3.1. Periodogram Analysis

Figure 3(a, b, c) represent the FFT, MEM and Scargle spectrum of 3–6 KeV RHESSI channel and the corresponding results are given in Table 1.

Figures 4 (a, b, c) represent the FFT, MEM and Scargle spectrum of 6-12 KeV RHESSI data and the corresponding results are given in Table 2.

Figures 5 (a, b, c) represent the FFT, MEM and Scargle spectrum of 12-25 KeV RHESSI data and the corresponding results are given in Table 3. Thus we find, in all methods and in all energy bands, the common periods to be  $\sim 71$  sec ( $P_1$ ) and  $\sim 53$  sec ( $P_2$ ). However, for the energy band of 12–25 KeV, an additional period  $\sim 39$  sec ( $P_3$ ) is found in all spectral decomposition techniques. The period ratios are estimated as  $P_1/P_2 = 71/53 \sim 1.339$ ;  $P_1/2P_2 \sim 0.669$ ;  $P_1/P_3 = 71/39 \sim 1.82$  or  $P_3/P_1 \sim 0.549$ .

#### 3.2. Cross-correlation Analysis

We also study lagging and leading behaviors of RHESSI 3–6 KeV, 6–12 KeV and 12–25 KeV channels during the decay phase of the flare by the cross-correlation technique and the plots are displayed in Figures 6(a, b, c). It is detected that there is no lag/lead between different energy channels demonstrating very high correlation of the signals in all observational bands. From figure

Table 1: List of periods detected with their Standard Errors for Confidence Limits in the decay phase of solar flare in energy band 3 - 6 KeV

Energy band		Identified spectral peaks (sec)		
		1	2	3
<b>(a) By FFT</b>				
3-6 KeV	T <sub>ave</sub>	71.56	53.34	38.62
	SE <sub>m</sub>	0.035	0.0195	0.0101
	T	71.56 ± 0.0903	53.34 ± 0.0503	38.62 ± 0.0261
	<b>(b) By MEM</b>			
	T <sub>ave</sub>	53.36	71.74	32.71
	SE <sub>m</sub>	0.274	0.457	0.102
	T	53.36 ± 0.7069	71.74 ± 1.1791	32.71 ± 0.2632
<b>(c) By Scargle Technique</b>				
	T <sub>ave</sub>	71.89	53.47	38.80
	SE <sub>m</sub>	0.0352	0.0192	0.0101
	T	71.89 ± 0.0908	53.47 ± 0.0495	38.80 ± 0.0260

Table 2: List of periods detected with their Standard Errors for Confidence Limits in the decay phase of solar flare in energy band 6 - 12 KeV

Energy band		Identified spectral peaks (sec)	
		1	2
<b>(a) By FFT</b>			
6-12 KeV	T <sub>ave</sub>	71.96	53.34
	SE <sub>m</sub>	0.0363	0.0203
	T	71.96 ± 0.0937	53.34 ± 0.0524
	<b>(b) By MEM</b>		
	T <sub>ave</sub>	71.80	53.43
	SE <sub>m</sub>	0.479	0.2803
	T	71.80 ± 1.2358	53.43 ± 0.7232
<b>(c) By Scargle Technique</b>			
	T <sub>ave</sub>	71.73	53.41
	SE <sub>m</sub>	0.0354	0.0183
	T	71.73 ± 0.0913	53.41 ± 0.0472

Table 3: List of periods detected with their Standard Errors for Confidence Limits in the decay phase of solar flare in energy band 12 – 25 KeV

Energy band		Identified spectral peaks (sec)			
		1	2	3	4
<b>(a) By FFT</b>					
12-25 KeV	T <sub>ave</sub>	71.08	53.14	38.88	
	SE <sub>m</sub>	0.0312	0.0185	0.0106	
	T	71.08 ± 0.0903	53.34 ± 0.0503	38.88 ± 0.0273	
	<b>(b) By MEM</b>				
	T <sub>ave</sub>	71.52	53.36	32.69	39.76
	SE <sub>m</sub>	0.537	0.278	0.104	0.213
	T	71.52 ± 1.385	53.36 ± 0.7172	32.69 ± 0.2683	39.76 ± 0.5495
<b>(c) By Scargle Technique</b>					
	T <sub>ave</sub>	72.15	53.60	38.78	
	SE <sub>m</sub>	0.0367	0.018	0.0104	
	T	72.15 ± 0.0947	53.60 ± 0.0464	38.78 ± 0.0268	

6 (a), it is detected that maximum cross-correlation coefficient is  $0.68 \pm 0.0168$  at 0 second. Figure 6 (b) exhibits that maximum cross-correlation coefficient is  $0.643 \pm 0.0195$  at 0 second. The maximum cross-correlation coefficient is  $0.781 \pm 0.0264$  at 0 second between the energy range 6–12 KeV and 12–25 KeV (Fig. 6c).

### 3.3. Morphology of the Flaring Loop System

GOES SXI image of the active region and its loop system beneath where the flare occurred is shown in Fig. 7 (right panel), while the same active region in 17 GHz NoRH observations is also displayed in Fig. 7 (left panel). The North-South axis in the GOES map is inclined for approximately 20 degrees clockwise relatively to the vertical direction. Therefore NoRH map shows the true position of the AR while GOES SXI image shows the rolled partial view. The soft X-ray enhancement occurred in the loop system during the evolution of the solar flare. The length of the flaring loop system is derived as  $L \sim 190$  Mm while its width is  $\sim 12$  Mm. The magnetic configuration of the flaring site obtained for 01:00 UT when approximate loop-length and width are derived, remains almost the same and changes insignificantly in 20 min later when QPOs evolve in the X-ray light curves. The loop-length is estimated by tracking the pixels along the loop. However, it should be noted that the estimated length is the lower bound projected length. The loop width is also estimated across the loop near its apex.

## 4. Results and Discussion

The observed periods are most likely associated with the first two harmonics of the fast magnetoacoustic wave modes in the flaring loop system. The phase

speed of the fundamental mode of magnetoacoustic wave is  $V_{ph} = 2L/P \sim 5200$  km/s, which seems to lie with the fastest magnetoacoustic branch (tubular-mode) within the loop. Since the QPPs modulate the emissions coming from the flaring loop system, they are compressible fast modes known as fast magnetoacoustic sausage modes.

The dispersion relation of fast-sausage waves in straight cylindrical tube includes both trapped and leaky modes depending on the plasma and magnetic field parameters (Edwin & Roberts, 1983).

The cut-off wavenumber  $k_c$  is written as given by Edwin & Roberts (1983) and Roberts et al. (1984):

$$k = k_c = \left[ \frac{V_A^2}{V_{Ae}^2 - V_A^2} \right]^{1/2} \frac{j_0}{a}, \quad (4)$$

where  $V_A$  and  $V_{Ae}$  are Alfvén speeds inside and outside the loop,  $a$  is the loop radius and  $j_0 = 2.4$  is the first zero of the Bessel function. The modes with  $k > k_c$  are trapped in the loop system, while the modes with  $k < k_c$  are leaky. The trapped fundamental global sausage mode ( $P = 72$  s) can be realized in this loop system only if the density contrast is:

$$\frac{L}{2a} < \frac{\pi V_{Ae}}{2j_0 V_{Ao}} \approx 0.65 \sqrt{\frac{\rho_o}{\rho_e}}, \quad (5)$$

which is equal to 593 for a given loop length  $L \sim 190$  Mm and width  $a \sim 6$  Mm. Therefore, the observed flaring loop must be very thick loop with significant density contrast to possess the global sausage modes. The maximum phase speed of the sausage wave 5200 km/s is considered as an external Alfvén speed ( $V_{Ae}$ ), while  $V_{Ao}$  is the internal Alfvén speed within the denser loop system. Using Eq. (2), we can estimate the ratio of external and internal Alfvén speed ( $V_{Ae}/V_{Ao}$ ) in the loop system as  $\sim 24.0$ . The phase speed of the fundamental mode sausage wave ( $V_{ph}$ ) can be maximum limit to the external Alfvén speed, i.e.,  $V_{Ae} = V_{ph} \sim 5200$  km/s. Therefore, the internal Alfvén speed ( $V_{Ao}$ ) within the loop will be 216 km/s. The diagnosed internal Alfvén speed ( $V_{Ao}$ ) of the flaring loop system is 216 km/s. The Alfvén speed inside the bulky flaring loop is significantly less compared to that in the outside ambient medium. This is expected as the density of such loops is higher compared to the normal loops as well as ambient plasma. This loop system does not possess the global sausage modes with period greater than  $PGSM \sim 2\pi/k_c$   $V_{Ae} \sim 2L/V_{Ae} \sim 73.0$  s (Pascoe et al., 2007). It should be noted that  $L = \pi/k_c$ . The longest period of the trapped sausage mode can have the period of  $\sim 73$  s. The observed period of fundamental mode sausage waves is less than this maximum period. Therefore, this period and its harmonics are well accepted in the given morphology and density contrast of the loop system.

Further, we have also found zero time lag between different soft X-ray energy bands. This zero lag in all bands depicts the periodicity that the wave concurred by sausage mode is not a propagating wave, but it is standing wave in nature. Therefore, we basically observe fast MHD pulsation of short periods



excited due to flare activity in the flaring loop system. As a result, the observed denser loops can support the non-leaky, trapped global sausage mode in the estimated length and width as well as density contrast (Nakariakov et al., 2003; Aschwanden et al., 2004; Srivastava et al., 2008). Such flaring/post-flare loops usually have a very high density contrast of the order of  $10^2$ – $10^3$ . The density evolves very rapidly during the flare heating and makes such loops highly denser. The observed loops are the X-class flaring loops where large heating is likely to take place during the strong X-class flare. Therefore, the estimated high density contrast is likely to occur and also falls in the expected range. Thus, the trapped sausage mode is probably excited in the loop system.

The ratio between the periods of the fundamental and the first harmonics of sausage waves is equal to  $P_1/P_2 \sim 1.34$ , which is shifted from 2.0. Similar physical behavior is observed for the fast-kink oscillations (Verwichte et al., 2004; Van Doorselaere et al., 2007; De Moortel & Brady, 2007; White & Verwichte, 2012; Srivastava & Goossens, 2013), for sausage waves (Srivastava et al., 2008), and for slow waves (Srivastava & Dwivedi, 2010). The deviation of  $P_1/P_2$  from 2.0 in homogeneous loops is very small due to the wave dispersion (McEwan et al., 2006; Andries et al., 2005). However, longitudinal density stratification causes significant shift of  $P_1/P_2$  from 2.0 (Andries et al., 2005, 2009; McEwan et al., 2006; Van Doorselaere et al., 2007; Macnamara & Roberts, 2010, 2011; Luna-Cardozo et al., 2012, and references therein). The longitudinal variation of density in a coronal loop is the most likely cause for the departure of the observed period ratio of the sausage waves. However, magnetic field geometry may also play an important role in its deviation (Macnamara & Roberts, 2011). Macnamara & Roberts (2011) have shown in their analytical calculations that as  $V_{Ae}/V_{Ao}$  tends to infinity the period ratio of the sausage waves ( $P_1/2P_2$ ) approaching towards 0.5 in their slab-model. Normally, it should be equal to 1.0. Taking account of our observed parameters, we obtain a very high ( $\sim 24$ ) external to internal Alfvén speed ratio. The period ratio ( $P_1/2P_2$ ) is significantly less, i.e., 0.65. This observation is qualitatively in agreement with the analytical solution of Macnamara & Roberts (2011) that period ratio reduces significantly for higher Alfvén velocity ratios.

In the present work, we find that QPPs are most likely caused by the sausage modes, and therefore, based on their signature local plasma properties are diagnosed. However, there may be other possible mechanisms which may be potentially responsible for QPP modulation. A few examples may be cited as the periodic variations of the angle between the line-of-sight and magnetic field by weakly compressible kink waves (Cooper et al., 2003), or by excitation of QPPs by MHD oscillation of an external loop (Nakariakov & Melnikov, 2009). Recently, Kolotkov et al. (2015) have analyzed the multiple MHD modes during the impulsive phase of the same flare that was approximately 18 min before the time interval analyzed in our present paper and lasting for a few minutes only. The signatures of waves are revealed with the mean periods of 15, 45, and 100 s. The 15 s and 100 s period are associated with the MHD modes rapidly decaying within a few wave periods. They are interpreted as leaky sausage modes and the kink modes respectively. The 45 second periodicity showed rather non

decaying behavior and the period similar to the findings of our present paper. This example shows that in the flaring region, the plasma and magnetic field conditions are rapidly varying. Therefore, even a single flare energy release over different epoch in the given duration of the flare may give rise to the evolution of different MHD modes and their properties. These properties are highly linked to the local plasma and magnetic field conditions, and can be used in diagnosing highly variable atmosphere there.

**Acknowledgments** We are grateful to the anonymous reviewers for their valuable comments. P. Chowdhury acknowledges BK21 plus program of the National Research Foundation (NRF) funded by the Ministry of Education of Korea. The research R. Sych has been funded by Chinese Academy of Sciences President's International Fellowship Initiative, Grant No. 2015VMA014 and by a Russian Foundation for Basic Research, Grants 13-02-00044 and 14-02-91157.

## References

- Andries, J., Arregui, I., & Goossens, M. 2005, *Astrophys. J. Lett.* , 624, L57
- Andries, J., van Doorselaere, T., Roberts, B., et al. 2009, *Space Sci. Rev.* , 149, 3
- Anfinogentov, S., Nakariakov, V. M., Mathioudakis, M., Van Doorselaere, T., & Kowalski, A. F. 2013, *Astrophys. J.* , 773, 156
- Asai, A., Shimojo, M., Isobe, H., et al. 2001, *Astrophys. J. Lett.* , 562, L103
- Aschwanden, M. J. 1987, *Solar Phys.* , 111, 113
- Aschwanden, M. J., Nakariakov, V. M., & Melnikov, V. F. 2004, *Astrophys. J.* , 600, 458
- Burg, J. P. 1972, *Geophysics*, 37, 375
- Chowdhury, P., & Ray, P. C. 2006, *Mon. Not. Roy. Astron. Soc.* , 373, 1577
- Chowdhury, P., Khan, M., & Ray, P. 2009, *Advances in Space Research*, 43, 297
- Cooper, F. C., Nakariakov, V. M., & Tsiklauri, D. 2003, *Astron. Astrophys.* , 397, 765
- De Moortel, I., & Brady, C. S. 2007, *Astrophys. J.* , 664, 1210
- Edwin, P. M., & Roberts, B. 1983, *Solar Phys.* , 88, 179
- Erdélyi, R., Hague, A., & Nelson, C. J. 2014, *Solar Phys.* , 289, 167
- Guo, Y., Erdélyi, R., Srivastava, A. K., et al. 2015, *Astrophys. J.* , 799, 151

- Haber, H., Runyon, R.P., 1969, General Statistics, Addison-Wesley, Reading, MA, p. 192
- Huang, J., Tan, B., Zhang, Y., Karlický, M., & Mészáros, H. 2014, *Astrophys. J.* , 791, 44
- Horne, J. H., & Baliunas, S. L. 1986, *Astrophys. J.* , 302, 757
- Inglis, A. R., Nakariakov, V. M., & Melnikov, V. F. 2008, *Astron. Astrophys.* , 487, 1147
- Inglis, A. R., van Doorselaere, T., Brady, C. S., & Nakariakov, V. M. 2009, *Astron. Astrophys.* , 503, 569
- Inglis, A. R., & Nakariakov, V. M. 2009, *Astron. Astrophys.* , 493, 259
- Jakimiec, J., & Tomczak, M. 2008, Central European Astrophysical Bulletin, 32, 65
- Kim, S., Nakariakov, V. M., & Shibasaki, K. 2012, *Astrophys. J. Lett.* , 756, L36
- Kolotkov, D. Y., Nakariakov, V. M., Kupriyanova, E. G., Ratcliffe, H., & Shibasaki, K. 2015, *Astron. Astrophys.* , 574, A53
- Kupriyanova, E. G., Melnikov, V. F., & Shibasaki, K. 2013, *Pub. Astron. Soc. Japan* , 65, 3
- Kupriyanova, E. G., Melnikov, V. F., Nakariakov, V. M., & Shibasaki, K. 2010, *Solar Phys.* , 267, 329
- Luna-Cardozo, M., Verth, G., & Erdélyi, R. 2012, *Astrophys. J.* , 748, 110
- Macnamara, C. K., & Roberts, B. 2010, *Astron. Astrophys.* , 515, A41
- Macnamara, C. K., & Roberts, B. 2011, *Astron. Astrophys.* , 526, A75
- Mathioudakis, M., Seiradakis, J. H., Williams, D. R., et al. 2003, *Astron. Astrophys.* , 403, 1101
- McAteer, R. T. J., Gallagher, P. T., & Ireland, J. 2005, *Astrophys. J.* , 631, 628
- McEwan, M. P., Donnelly, G. R., Díaz, A. J., & Roberts, B. 2006, *Astron. Astrophys.* , 460, 893
- Melnikov, V. F., Reznikova, V. E., Shibasaki, K., & Nakariakov, V. M. 2005, *Astron. Astrophys.* , 439, 727
- Mitra-Kraev, U., Harra, L. K., Williams, D. R., & Kraev, E. 2005, *Astron. Astrophys.* , 436, 1041
- Nakariakov, V. M., Melnikov, V. F., & Reznikova, V. E. 2003, *Astron. Astrophys.* , 412, L7

- Nakariakov, V. M., & Verwichte, E. 2005, *Living Reviews in Solar Physics*, 2, 3
- Nakariakov, V. M., & Melnikov, V. F. 2009, *Space Sci. Rev.* , 149, 119
- Orza, B., & Ballai, I. 2013, *Astronomische Nachrichten*, 334, 948
- Pandey, J. C., & Srivastava, A. K. 2009, *Astrophys. J. Lett.* , 697, L153
- Pascoe, D. J., Nakariakov, V. M., & Arber, T. D. 2007, *Solar Phys.* , 246, 165
- Reznikova, V. E., Melnikov, V. F., Su, Y., & Huang, G. 2007, *Astronomy Reports*, 51, 588
- Reznikova, V. E., & Shibasaki, K. 2011, *Astron. Astrophys.* , 525, A112
- Roberts, B., Edwin, P. M., & Benz, A. O. 1984, *Astrophys. J.* , 279, 857
- Scargle, J. D. 1982, *Astrophys. J.* , 263, 835
- Srivastava, A. K., Zaqarashvili, T. V., Uddin, W., Dwivedi, B. N., & Kumar, P. 2008, *Mon. Not. Roy. Astron. Soc.* , 388, 1899
- Srivastava, A. K., & Dwivedi, B. N. 2010, *New Astr.*, 15, 8
- Srivastava, A. K., Lalitha, S., & Pandey, J. C. 2013, *Astrophys. J. Lett.* , 778, L28
- Srivastava, A. K., & Goossens, M. 2013, *Astrophys. J.* , 777, 17
- Sych, R., Nakariakov, V. M., Karlicky, M., & Anfinogentov, S. 2009, *Astron. Astrophys.* , 505, 791
- Sych, R., Karlicky, M., Altyntsev, A., Dudk, J. & Kashapova, L. 2009, *Astron. Astrophys.* , 577, A43
- Tan, B., Zhang, Y., Tan, C., & Liu, Y. 2010, *Astrophys. J.* , 723, 25
- Van Doorselaere, T., Nakariakov, V. M., & Verwichte, E. 2007, *Astron. Astrophys.* , 473, 959
- Verwichte, E., Nakariakov, V. M., Ofman, L., & Deluca, E. E. 2004, *Solar Phys.* , 223, 77
- White, R. S., & Verwichte, E. 2012, *Astron. Astrophys.* , 537, A49

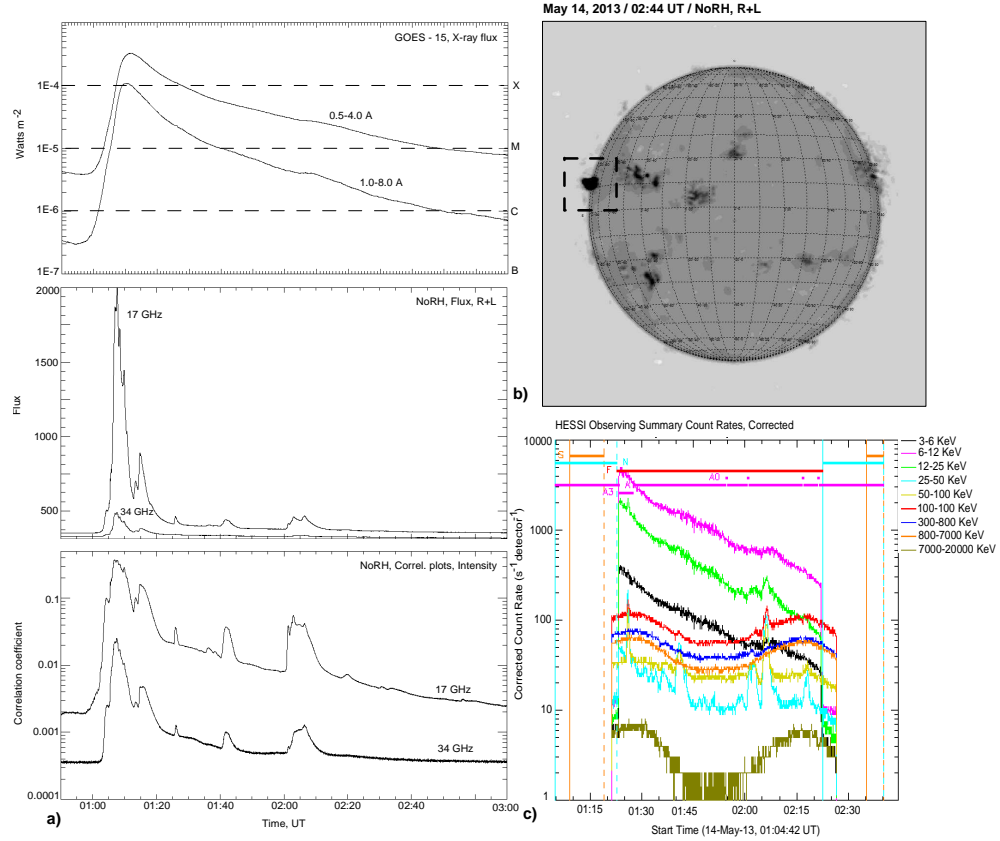


Figure 1: (a) GOES plot showing temporal evolution of soft X-rays (top panel). The microwave emission measured by NoRH at 17 and 34 GHz - integral flux (middle panel) and correlation plots (bottom panel). (b) Full Sun in intensity NoRH channel at 17 GHz. The flare region is indicated by the solid box. (c) Localized temporal span of the light curves of different energy bands during the decay phase of the flare detected by RHESSI on May 14, 2013

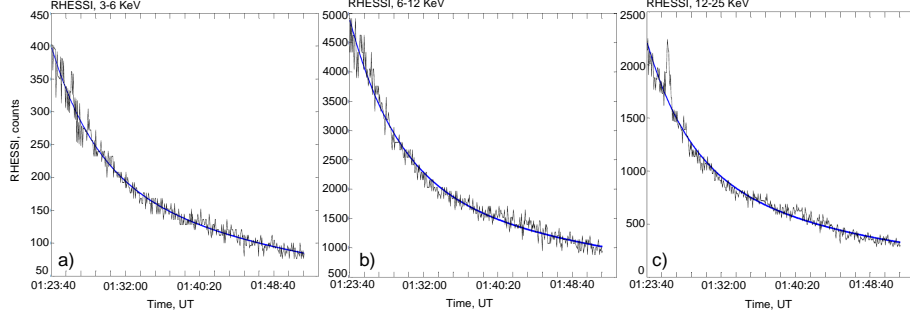


Figure 2: RHESSI soft X-ray light curves on May 14, 2013, from 01:23:40 to 01:51:56 UT. (a) Blue line is the trend fitting X-ray light curve for 3–6 Kev data; (b) same for energy band 6–12 keV and (c) same for energy band 12–25 Kev.

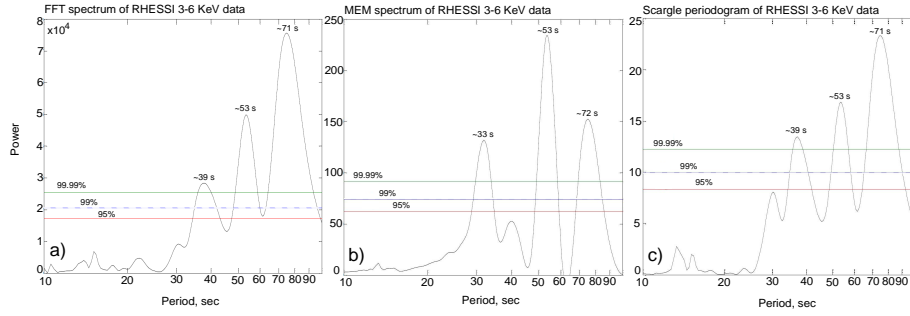


Figure 3: (a) FFT spectra of RHESSI 3–6 Kev data; (b) MEM spectra for the same data and (c) Scargle spectra of the same data.

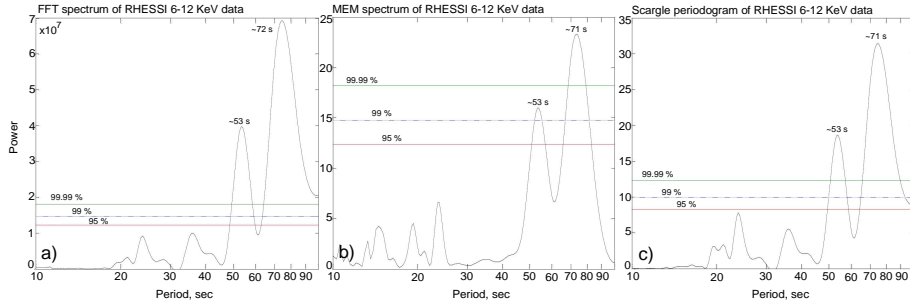


Figure 4: (a) FFT spectra of RHESSI 6–12 Kev data; (b) MEM spectra for the same data and (c) Scargle spectra of the same data.

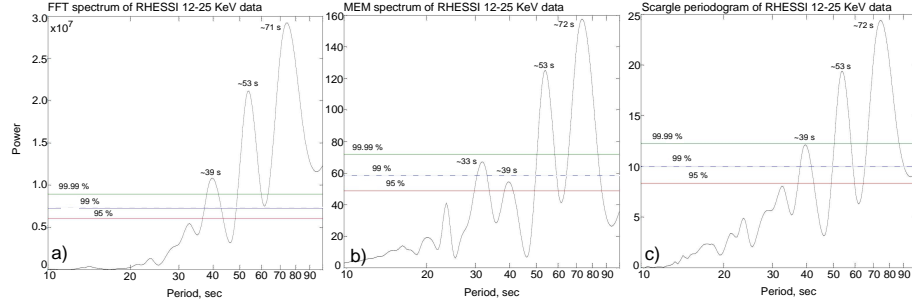


Figure 5: (a) FFT spectra of RHESSI 12–25 Kev data; (b) MEM spectra for the same data and (c) Scargle spectra of the same data.

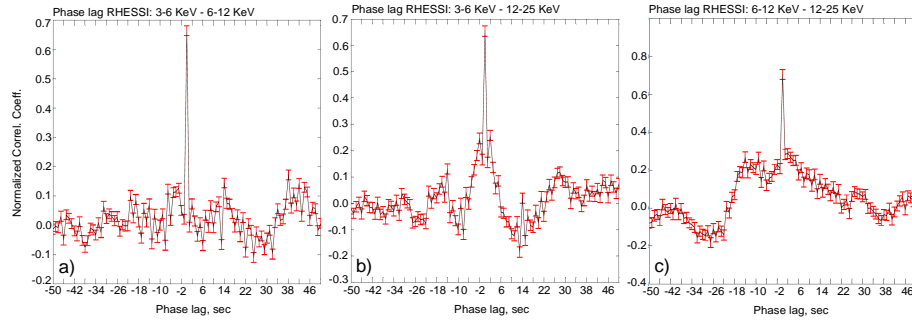


Figure 6: (a) Cross-correlation analysis between RHESSI 3–6 and 6–12 Kev data sets ; (b) Cross-correlation analysis between RHESSI 3–6 and 12–25 Kev data ; (c) Cross-correlation analysis between RHESSI 6–12 and 12–25 Kev data set.

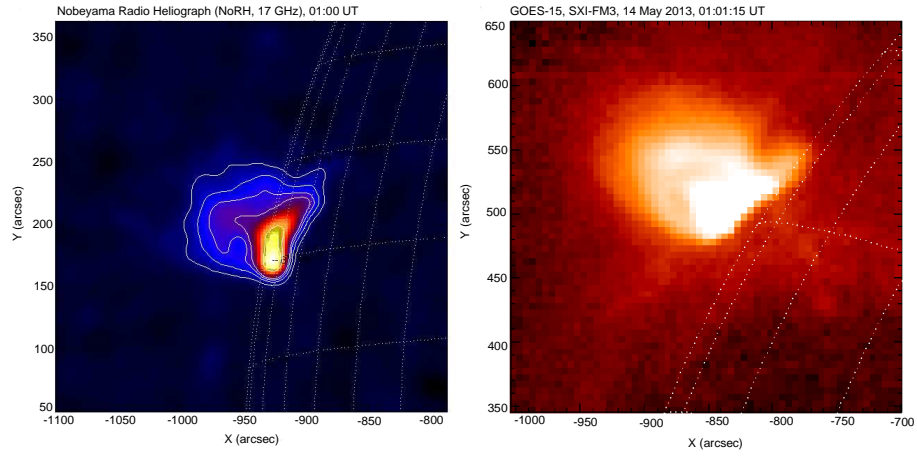


Figure 7: Left-panel : NoRH image showing the position of flaring active region. Right-panel : Partial view of the GOES SXI image of X-class flaring region (negative color image) and loop system beneath which the flare occurred. The soft X-ray enhancement occurred in the loop system is shown during the evolution of the solar flare. The North-South axis in the GOES map is inclined for approximately 20 degrees clockwise relative to the vertical direction. Therefore NoRH map shows the true position of the AR while GOES SXI image shows the rolled partial view.